Study for material analogs of FeSb$_2$: Material design for thermoelectric materials

Chang-Jong Kang[1,*] and Gabriel Kotliar[1,2]

[1]*Department of Physics and Astronomy, Rutgers University, Piscataway, New Jersey 08854, USA*
[2]*Condensed Matter Physics and Materials Science Department, Brookhaven National Laboratory, Upton, New York 11973, USA*

Using the *ab initio* evolutionary algorithm (implemented in USPEX) and electronic structure calculations we investigate the properties of a new thermoelectric material FeSbAs, which is a material analog of the enigmatic thermoelectric FeSb$_2$. We utilize the density functional theory and the Gutzwiller method to check the energetics. We find that FeSbAs can be made thermodynamically stable above ∼30 GPa. We investigate the electronic structure and thermoelectric properties of FeSbAs based on the density functional theory and compare with those of FeSb$_2$. Above 50 K, FeSbAs has higher Seebeck coefficients than FeSb$_2$. Upon doping, the figure of merit becomes larger for FeSbAs than for FeSb$_2$. Another material analog FeSbP, was also investigated, and found thermodynamically unstable even at very high pressure. Regarding FeSb$_2$ as a member of a family of compounds (FeSb$_2$, FeSbAs, and FeSbP) we elucidate what are the chemical handles that control the gaps in this series. We also investigate solubility (As or P for Sb in FeSb$_2$) we found As to be more soluble. Finally, we study a two-band model for thermoelectric properties and find that the temperature dependent chemical potential and the presence of the ionized impurities are important to explain the extremum in the Seebeck coefficient exhibited in experiments for FeSb$_2$.

I. INTRODUCTION

The search for thermoelectric materials having large Seebeck coefficients has attracted lots of interest during the past several decades. Since these materials have efficiency for converting temperature differences in electric voltages, it could be used to make refrigerators or power generators [1]. Correlated semiconductors and Kondo insulators containing rare-earth or transition metal atoms have been regarded as the possible candidates for good thermoelectric materials due to a sharp singularity in the density of states very near to the chemical potential [2–5].

In order to get high efficiency or performance in the thermoelectric materials for applications, it is necessary to increase the (dimensionless) figure of merit as much as possible,

$$ZT = \frac{\sigma S^2}{\kappa_e + \kappa_l} T, \qquad (1)$$

where σ is the electrical conductivity, S is the Seebeck coefficient (also known as thermoelectric power), κ_e and κ_l are the thermal conductivities that are contributed from the electronic part and the lattice part, respectively. Note that the numerator in Eq. (1) is called as the thermoelectric power factor ($PF = \sigma S^2$). Therefore the large thermoelectric power factor with the small thermal conductivities gives the high figure of merit.

A correlated semiconductor FeSb$_2$ was reported to have a gigantic Seebeck coefficient $S = -45$ mV/K at ∼12 K [6,7], which results in the largest PF ever found (∼65 times larger than the PF of the state-of-the-art thermoelectric Bi$_2$Te$_3$-based material [3]). However, the lattice thermal conductivity κ_l

reaches a maximum as large as ∼500 W m^{-1} K^{-1} at ∼15 K [6,7]. It leads to a quite small ZT value of 0.005 at the maximum of the PF. Considering the fact that any material with $ZT > 1$ is of great technological interest, it is worth to try to reduce κ_l significantly without seriously affecting the PF.

The previous theoretical studies of FeSb$_2$ reported that the gigantic Seebeck coefficient at low temperature could not be described within both the density functional theory (DFT) level and a local electronic picture [8,9], suggesting the substantial effect due to phonon drag [10,11] or the importance of vertex corrections [8], the latter was attributed to the impurity band [12]. In this paper, we have focused on the moderate temperature range (above ∼50 K) where vertex corrections or phonon drag effect are not so important and could be safely ignored. Our aim in this work is to explore structural analogs of FeSb$_2$. A natural question is, what will be the effect of substituting Sb by P or As? We find that the As substitution is much more favorable. At ambient pressure As is more soluble than P. High pressure can stabilize FeSbAs, but FeSbP is not stable even at very high pressure. P substitution decreases the gap and the thermoelectric properties, however, As substitution increases the gap and the Seebeck coefficient and is a good target for synthesis. In the process of designing these materials we identify the octahedral rotations that control the size of the band gap in the marcasite structure.

Modern theoretical methods of structure prediction have been very successful in finding new interesting materials experimentally. Even though DFT has computational errors to determine the formation energy of a compound [13,14], various corrections have been designed and implemented in searchable repositories of DFT databases such as Material Project [15], OQMD [14], and AFLOWlib [16]. They give useful guideline to experiments for material synthesis and

*ck620@physics.rutgers.edu

design. Notable recent successes are the prediction of the 112 family of iron based superconductors [17–19] and the prediction of superconductivity of hydrogen sulfide that has the highest critical temperature under high pressure [20,21]. Other successes of theory guided material searches are the prediction and synthesis of unreported missing half-Heusler compounds, which are potential transparent conductors, thermoelectric materials, and topological semimetals [22–24]. In addition, new high-pressure phase materials such as FeO_2 [25], calcium carbides [26], and Na_2He [27] were predicted by theory and confirmed to exist by experiment. (For details of computational predictions based on DFT, see the review [28].) This undoubtedly very partial list of accomplishments and references, shows the speed at which theory is becoming predictive and playing an important role in the search for new materials, and here we employ this methodology to enlarge the family of iron based marcasites and related structures.

II. METHOD

To obtain the stable structural phase of FeSbAs, we employ the *ab initio* evolutionary algorithm [29] implemented in USPEX [30] combined with DFT pseudopotential code VASP [31,32]. The initial structures are randomly generated according to possible space groups. In these calculations, the structural optimization of all the newly generated structures are carried out by VASP with an energy cutoff of 500 eV and the exchange-correlation functional of generalized gradient approximation (GGA) of Perdew-Burke-Ernzerhof (PBE) [33] with the projector augmented wave (PAW) method [34,35]. After stable structural phases are obtained, corresponding formation energies are calculated with the Monkhorst-Pack sampling grid with a uniform density of 3000 k point per atom for the k-space integrations.

To check the energetics more precisely but relatively cheap, we utilized the Gutzwiller method [36,37] combined with the all-electron full-potential linearized augmented plane-wave (FLAPW) method implemented in WIEN2K [38]. We employ the general Slater-Condon parametrization of the on-site interaction with $U = 5$ and a Hund's coupling constant $J = 0.7$ eV, which were turned out to be reliable parameters in Fe compounds [39,40].

Both LDA (local-density approximation) and GGA(PBE) functionals tend to underestimate band gaps of semiconductors. To obtain the electronic structures with a reasonable band gap, we utilized the modified Becke-John (mBJ) exchange potential [41], which is rather accurate and computationally cheaper than the GW method. We sampled the entire Brillouin zone (BZ) with $18 \times 16 \times 32$ k points.

The calculation of transport properties was performed using a denser mesh of $45 \times 40 \times 80$ k points of the BZ. The semiclassical Boltzmann theory as implemented in the transport code BOLTZTRAP [42] has been used to compute the electrical transport coefficients.

III. COMPUTATIONAL RESULTS AND DISCUSSION

A. Crystal structure and phase stability

The crystal structure of $FeSb_2$ is shown in Fig. 1(a), which has the orthorhombic marcasite structure (space group: *Pnnm*)
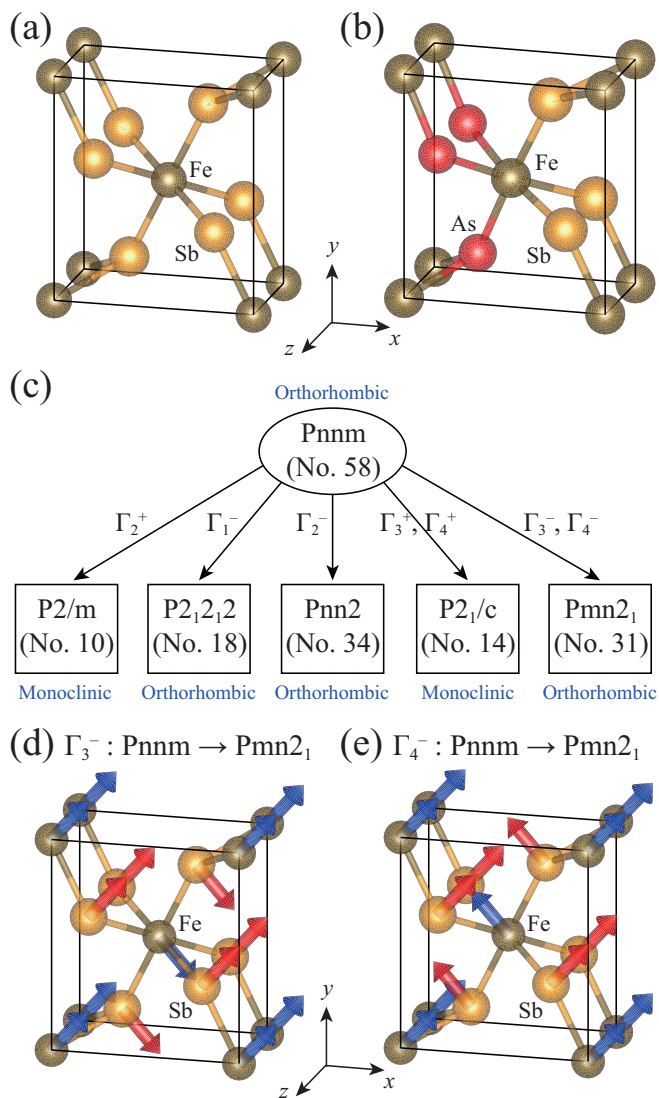

FIG. 1. (a) Crystal structure of $FeSb_2$. The space group is *Pnnm* (No. 58). (b) Crystal structure of FeSbAs. The space group is *Pmn2₁* (No. 31). The crystal axes are reoriented for easily comparison with the crystal structure of $FeSb_2$. The black lines represent the unit cell in both (a) and (b). (c) Group table related to the Marcasite structure (*Pnnm*). The structural phase transition between *Pnnm* and *Pmn2₁* is related to the (d) Γ_3^- or (e) Γ_4^- symmetries of the lattice distortions. The arrows indicate atomic displacements in the reference structure of *Pnnm*.

where a Fe ion is surrounded octahedrally by six Sb anions [43]. The Fe octahedron has corner sharing with the neighboring Fe octahedron in an x-y plane, however it has edge sharing along the z direction. Therefore, it is expected to have larger band dispersion along the z direction than x or y directions (see Fig. 3). The crystal structure of FeSbAs at ambient or under pressures founded by USPEX has a space group *Pmn2₁*, and it can be interpreted as the structural phase transition from the space group *Pnnm* with the Γ_3^- or Γ_4^- symmetries of the lattice distortions as shown in Fig. 1(c). These Γ_3^- or Γ_4^- lattice distortions are confined within the x-y plane and lead to break the inversion symmetry (the replacement of three Sb with three As atoms breaks the inversion symmetry as well). The

TABLE I. Relaxed structural parameters of FeSb$_2$ (space group: $Pnnm$), FeSbAs (space group: $Pmn2_1$), and FeSbP (space group: $Pmn2_1$). The crystal axes for FeSbAs and FeSbP are reoriented to have the space group of $Pn2_1m$ in order to compare with $Pnnm$ easily.

	FeSb$_2$ $P = 0$	FeSbAs $P = 0$ (40 GPa)	FeSbP $P = 0$
Space group	$Pnnm$	Pn2$_1$m	Pn2$_1$m
a (Å)	5.761	5.555 (5.250)	5.366
b (Å)	6.512	6.265 (5.884)	6.097
c (Å)	3.297	3.051 (2.797)	3.001
Wyckoff positions			
Fe	2a	2a	2a
	$x = 0.000$	$x = 0.774\ (0.772)$	$x = 0.792$
	$y = 0.000$	$y = 0.000\ (0.000)$	$y = 0.000$
Sb	4g	2a	2a
	$x = 0.198$	$x = 0.571\ (0.574)$	$x = 0.578$
	$y = 0.355$	$y = 0.365\ (0.364)$	$y = 0.375$
As (P)	–	2a	2a
		$x = 0.942\ (0.937)$	$x = 0.945$
		$y = 0.651\ (0.653)$	$y = 0.656$

structural information on FeSbAs at ambient or under pressure could be found in Table I along with FeSb$_2$ for comparison.

FeSbAs at ambient pressure is thermodynamically unstable and decomposed into FeAs and Sb compounds. The energy above hull is 32.2 meV/atom. We have checked the phase stability of FeSbAs under pressures dealing with the enthalpy $H = E + PV$, where E is the total electronic energy, P is the external pressure, and V is the crystal volume. Three relevant reactions for FeSbAs under pressures are shown in Fig. 2(c), where the enthalpy of formation ΔH is plotted as a function of pressure. The positive or negative enthalpy of formation indicates that FeSbAs is thermodynamically unstable or stable, respectively. Two reactions such as FeSb$_3$ + FeAs$_2$ + FeAs $\rightarrow$ 3 FeSbAs and FeAs + Sb $\rightarrow$ FeSbAs are stable above ∼8 GPa, however FeSb$_2$ + FeAs$_2$ $\rightarrow$ 2 FeSbAs is only stable at high pressure ($P \geqslant 30$ GPa). Therefore the reaction process of FeSb$_2$ + FeAs$_2$ $\rightarrow$ 2 FeSbAs is an indicator of the phase stability of FeSbAs (the detail enthalpy for each material is listed in Table II). We also checked the phase stability of FeSbAs with the GGA(PBE) + Gutzwiller (GUTZ), which is the advanced but relatively cheap method for doing energetics. The GGA + GUTZ method describes the smaller pressure to stabilize FeSbAs compared to DFT GGA(PBE) method. The LDA + GUTZ method is also tested because LDA + GUTZ gives better energetics than GGA + GUTZ. With LDA + GUTZ, it gives the stable phase of FeSbAs above 30 GPa, which is quite close to the DFT GGA(PBE) result (not shown). Hence it is safe to mention that FeSbAs is only stable above $P \sim 30$ GPa, and FeSbAs is decomposed into FeSb$_2$ and FeAs$_2$ compounds below the pressure.

Even though FeSbAs is thermodynamically stable only at high pressure (above ∼30 GPa), we checked the phonon dispersion of FeSbAs at ambient pressure and found that it is mechanically stable (no imaginary phonon softening). It is the similar situation in diamond: diamond is less thermodynamically stable than graphite, however is mechanically
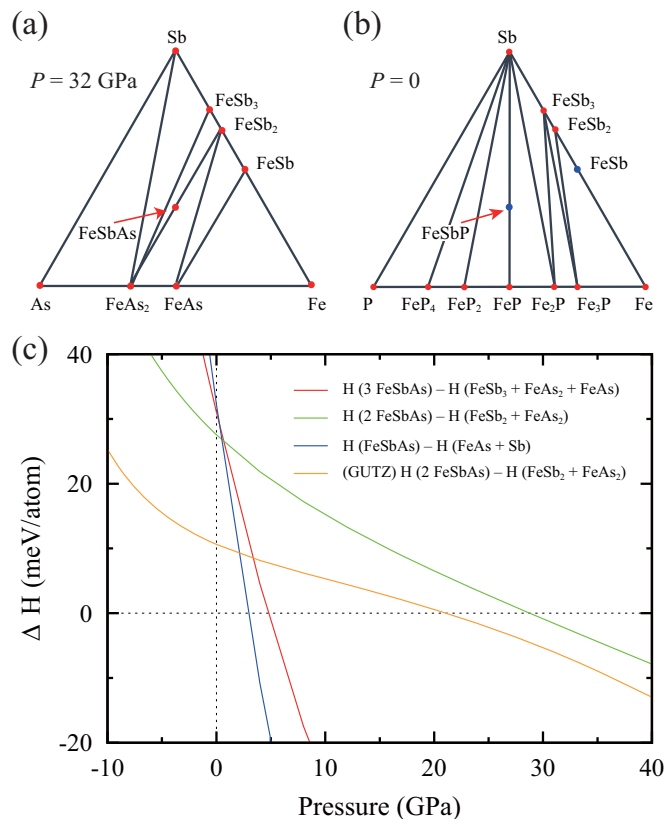

FIG. 2. (a) Ternary phase diagram for FeSbAs under the pressure of 32 GPa. FeSbAs is thermodynamically unstable at ambient pressure and is only stable at high pressures ($P \geqslant 30$ GPa). (b) Ternary phase diagram for FeSbP at ambient pressure. Red and blue dots represent thermodynamically stable and unstable phase, respectively. The energy above hull for FeSbP is 204.6 meV/atom. Ternary phase diagrams are generated by pymatgen [44–46]. (c) Enthalpy of formation for FeSbAs. In order to obtain the enthalpy of formation as a function of pressure, several lattice volumes including the optimized one were calculated, and then the Murnaghan fitting was applied to extract the enthalpy of formation at any pressure. The relevant reaction for the stability of FeSbAs is FeSb$_2$ + FeAs$_2$ $\rightarrow$ 2 FeSbAs. We also checked the stability of this reaction by using the GGA(PBE) + Gutzwiller (GUTZ) method. The GUTZ method describes the smaller pressure to stabilize FeSbAs compared to DFT GGA(PBE) method.

stable at ambient pressure. Once FeSbAs is synthesized at high pressures, it could be released into ambient pressure without decomposing into other substances (assuming that the conversion rate from FeSbAs to other substances is negligible at standard conditions).

Another material analog FeSbP is also tested. First, USPEX was performed to search the crystal structure for FeSbP. The space group $Pmn2_1$ (No. 31) was obtained, which is same as one for FeSbAs. FeSbP at ambient pressure is thermodynamically unstable and decomposed into FeP and Sb compounds [Fig. 2(b)]. The energy above hull is 204.6 meV/atom, which is much larger than that for FeSbAs at ambient pressure. It indicates that FeSbP is more thermodynamically unstable than FeSbAs. We have checked the phase stability of FeSbP under pressures and found that FeSbP is unstable over the whole pressure range (even at high pressure).

TABLE II. Enthalpy for each material exhibited in Figs. 2(a) and 2(b) at $P = 0$ or 32 GPa calculated by VASP GGA(PBE) functional.

	Enthalpy $H = E + PV$ (eV/atom)	
	$P = 0$ GPa	$P = 32$ GPa
Fe	−8.236	−6.100
Sb	−4.138	1.185
As	−4.672	−0.784
FeSb	−6.171	−2.962
FeSb$_2$	−5.534	−1.855
FeSb$_3$	−5.189	−1.134
FeAs	−6.681	−4.181
FeAs$_2$	−6.123	−3.313
FeSbAs	−5.801	−2.586
P	−5.404	−1.242
Fe$_3$P	−7.797	−5.754
Fe$_2$P	−7.767	−5.718
FeP	−7.425	−5.294
FeP$_2$	−6.886	−4.522
FeP$_4$	−6.345	−3.664
FeSbP	−6.125	−3.132

Hereafter, we will discuss the electronic structure and thermoelectric properties for FeSbAs at high pressure $P = 40$ GPa unless otherwise noted. For FeSbP, there is no any pressure to stabilize it, but the ambient pressure phase is chosen to study the electronic structure and thermoelectric properties in order to compare with other material analogs.

B. Electronic structure

Figure 3 shows band structures of FeSb$_2$, FeSbAs, and FeSbP with the structural parameters exhibited in Table I. All the materials FeSb$_2$, FeSbAs, and FeSbP show the metallic phase based on the GGA(PBE) functional. The standard DFT describes severe underestimation of a bulk band gap, so that DFT + U, hybrid functional, or GW are required to obtain the proper bulk band gap.

First, we checked the GGA + U (the on-site Coulomb repulsion parameter) method with an effective $U_{\mathrm{eff}} = U - J$ parameter setting $J = 0$. For $U_{\mathrm{eff}} = 4$ eV, the band gap of FeSb$_2$ is 166 meV, which is almost five times larger than the experimental band gap of ∼30 meV [6,47,48]. While FeSb$_2$ is paramagnetic in experiments, the GGA + U method describes that the ferromagnetic solution has the lower energy than the

nonmagnetic solution [49]. Therefore the GGA + U method is not suitable to study the electronic structure of FeSb$_2$.

The mBJ method was thoroughly tested for many semiconductors and insulators to obtain band gaps close to the experimental ones [41]. The band gap of FeSb$_2$ described in mBJ is 19 meV, which is very close to the experimental data of ∼30 meV. Thus, in view of a much reduced computational time compared to the GW [8], mBJ is indeed an efficient method to get a reasonable band gap and proper thermoelectric properties at the moderate temperature range above 50 K. (At low temperature, the vertex correction is inevitable to get the reasonable thermoelectric power. Here, we have focused on the moderate temperature range above 50 K where the vertex correction or phonon-phonon interaction are not so important.) For the case of FeSbAs, mBJ gives the band gap of 146 meV, which is quite large compared to the FeSb$_2$ case. On the other hand, FeSbP is a compensated semimetal within the mBJ scheme. The valence band along Γ-X and the conduction band along Γ-Z cross the Fermi level, which results in giving hole and electron pockets, respectively.

The size of the band gap is closely related to a rotation angle θ [Fig. 4(b)] of the Fe octahedron around the z axis. At zero rotation angle, the band gap is closed as shown in Fig. 4(c) due to large hopping integrals between Fe and Sb atoms. The band gap begins to open at a certain amount of the rotation angle (so-called θ_0), and it increases further to get the maximum and then decreases as the rotation angle increases. The rotation angle θ_0 could differ depending on the anion size and the crystal unit cell volume. The rotation angles in the equilibrium structures for FeSb$_2$, FeSbAs, and FeSbP are 15.2°, 18.2°, and 19.1°, respectively [Fig. 4(e)]. If the rotation angle is increased further to be 20° in FeSb$_2$, the band gap is also increased further and its magnitude is 0.48 eV [Figs. 4(d) and 4(f)]. For FeSbP, the band gap starts to open at $\theta_0 \approx 20°$, which is larger than θ_0 for other two materials as shown in Fig. 4(f).

Since a larger bulk gap material usually gives a larger high-temperature thermoelectric power [8], it is expected that the thermoelectric power for FeSbAs is the largest, FeSb$_2$ is the second, and FeSbP is the smallest among them.

C. Thermoelectric properties

The theoretically calculated thermoelectric power for FeSb$_2$ as a function of temperature is shown in Fig. 5(a) with the experimental data for comparison. We set the chemical potential to be the middle of the band gap. At low temperature
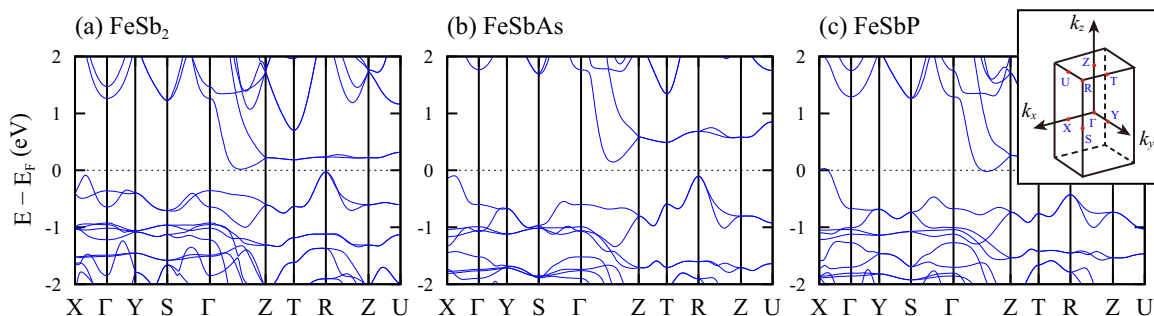

FIG. 3. Band structures of (a) FeSb$_2$, (b) FeSbAs, and (c) FeSbP calculated by the mBJ method. Inset shows the bulk Brillouin zone. The considered crystal structures are provided in Table I. For FeSbAs, the crystal structure at high pressure $P = 40$ GPa was chosen.
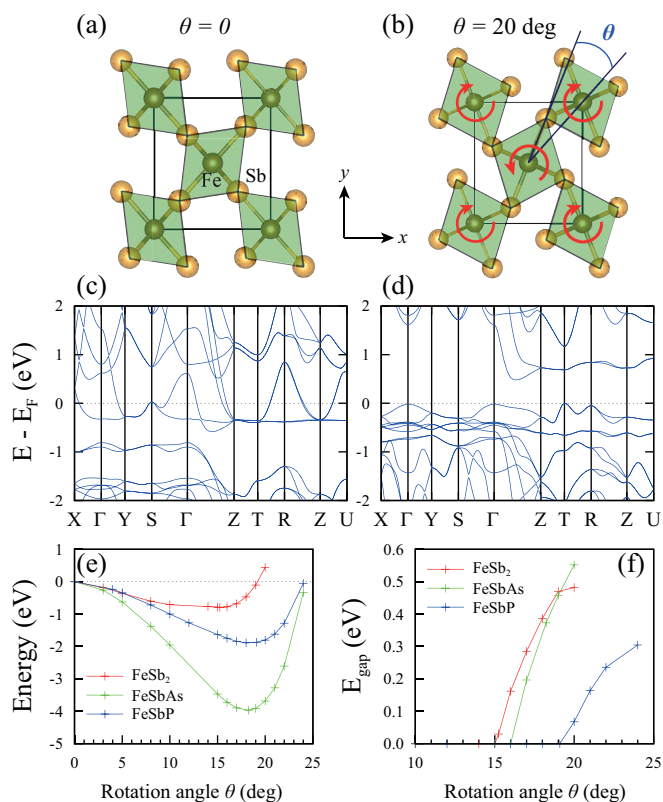
FIG. 4. Hypothetical crystal structure of FeSb$_2$ with an octahedron rotation angle (a) $\theta = 0°$ and (b) $\theta = 20°$ with keeping the space group *Pnnm* (No. 58). Fe (Sb) atoms are located in the center (corner) of the green-colored octahedrons. The corresponding electronic band structures of (a) and (b) calculated by the mBJ method are shown in (c) and (d), respectively. The band gap in (d) is indirect and its magnitude is 0.48 eV. (e) Energy vs rotation angle θ for FeSb$_2$, FeSbAs, and FeSbP calculated by the mBJ method. Energy for $\theta = 0°$ for each material is set to be zero as reference energy. Equilibrium rotation angles for FeSb$_2$, FeSbAs, and FeSbP are 15.2°, 18.2°, and 19.1°, respectively. (f) Band gap vs rotation angle θ for FeSb$_2$, FeSbAs, and FeSbP calculated by the mBJ method. The band gap could be controlled by the octahedron rotation.

below 50 K, the theoretically calculated thermoelectric power could not describe the gigantic thermoelectric power observed in experiments. This suggests that vertex corrections and nonlocal correlation effects that we neglect are important. The presence of a substantial phonon-drag effect could also give the huge inconsistency between experiments and the current theory.

Above ∼80 K, the calculated thermoelectric powers are well matched with the experiment in the sense that the thermoelectric powers described by both theory and experiment have the same order of magnitude (except for zz component) and have the same increasing tendency, that is, the same positive slope in the thermoelectric power versus temperature curve. However, there is a discrepancy in the thermoelectric power along zz direction (S_{zz}) between mBJ and the experiment: mBJ describes S_{zz} several times (from ∼4 to ∼8 times) larger than the experiment at the temperature range between 100 and 300 K. This discrepancy might come from the fixed chemical potential over the temperature range in the calculation. In
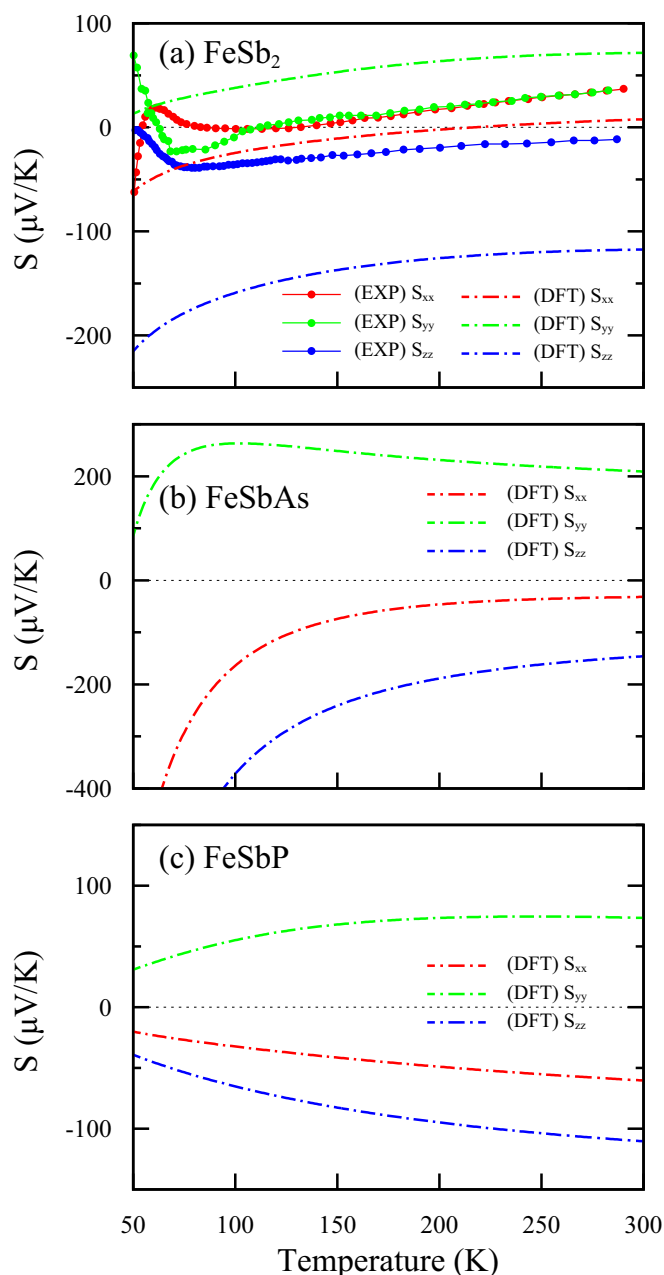

FIG. 5. (a) Thermoelectric power of FeSb$_2$ as a function of temperature. Experimental data from Ref. [6] are shown for comparison with DFT (mBJ potential method) results. Thermoelectric powers of (b) FeSbAs and (c) FeSbP calculated by DFT (mBJ method) as a function of temperature. The temperature range from 0 to 50 K is the unreliable region within the current theoretical approach (see main text for details), so that the moderate temperature region above 50 K is focused in this study.

addition, the several types of impurities such as electron donor or hole acceptor impurities could be also important to give better consistency between theory and experiment. We will discuss the temperature behavior of the thermoelectric power with the chemical potential varied with temperature and the effect of the presence of impurities in Appendix.

The thermoelectric power for FeSbAs is also calculated and shown in Fig. 5(b). The thermoelectric power for FeSbAs is

much enhanced compared to FeSb$_2$: ~6.7, ~6.9, and ~2.3 times enhanced in a magnitude along xx, yy, and zz directions, respectively, at $T = 100$ K. The Seebeck coefficients could be enhanced by the shift of the chemical potential, supposing that electron or hole doping does not alter the electronic structure heavily. The maximum value of the Seebeck coefficient could be achieved with 0.01–0.02 eV shift in the chemical potential. Then the Seebeck coefficient is about four times larger for FeSbAs than for FeSb$_2$ [see Fig. 7(a)]. Hence the newly proposed material FeSbAs has larger thermoelectric powers than FeSb$_2$ above 50 K.

Power factors (PFs) divided by the relaxation time (τ) calculated within mBJ for FeSb$_2$ are larger than those for FeSbAs above 50 K (Fig. 6). For example, at $T = 300$ K, they are 0.022 (0.03), 1.05 (0.88), and 3.05 (0.48) $\times 10^{12}$ W cm^{-1} K^{-2} s^{-1} for xx, yy, and zz directions, respectively, for FeSb$_2$ (FeSbAs). Even though Seebeck coefficients for FeSbAs are larger than for FeSb$_2$ above 50 K, the electrical conductivity (σ) for FeSbAs is smaller than for FeSb$_2$ due to the larger band gap, so that the resulting PF/τ ($= \sigma S^2/\tau$) for FeSbAs is smaller than for FeSb$_2$. However, if the chemical potential could be shifted through the doping without altering the electronic structure heavily, PF/τ for both FeSbAs and FeSb$_2$ are quite comparable at around 0.1 or around -0.1 eV shift of the chemical potential.

Since FeSbP has the metallic phase within the mBJ method, the linear temperature dependent thermoelectric power ($S \sim T$) is demonstrated at low temperature as shown in Fig. 5(c). The thermoelectric powers for FeSbP along xx, yy, and zz directions are confined below ~100 μV/K in magnitude at the temperature range between 50 and 300 K. They are much reduced compared to those for FeSbAs but are similar in size with those for FeSb$_2$ except for the zz component. FeSb$_2$ has the larger zz component than FeSbP and it leads to the larger average thermoelectric power for FeSb$_2$ than for FeSbP as shown in Fig. 7(a).

Even though the thermoelectric powers for FeSbP are smaller than those for FeSbAs, PF/τ for FeSbP is much larger than that for FeSbAs (~13 times larger at $T = 300$ K for the zz component) due to the larger σ of metallic FeSbP than that of insulating FeSbAs. However, PF/τ for both FeSbAs and FeSbP are quite comparable for the chemical potential shift larger than $+0.1$ eV.

Figure 7(b) shows the figure of merit ZT (here, only the electronic contribution to the thermal conductivity is considered) as a function of the chemical potential for three different materials FeSb$_2$, FeSbAs, and FeSbP. The figure of merit for FeSbAs is almost two times enhanced compared to that for FeSb$_2$. Considering that PF/τ for FeSbAs is smaller than for FeSb$_2$, this enhancement is due to the smaller electronic thermal conductivity (κ_e) in FeSbAs than in FeSb$_2$. (Since FeSbAs has a larger band gap than FeSb$_2$, it makes both σ and κ_e of FeSbAs smaller than those of FeSb$_2$.) For FeSbP, both σ and κ_e are large due to the metallic phase. It leads to a quite small figure of merit for FeSbP.

The electronic thermal conductivity could be calculated from the electrical conductivity by using the Wiedemann-Franz law with the Lorenz number $L_0 = 2.44 \times 10^{-8}$ W Ω K^{-2}. From the electrical conductivities of FeSb$_2$ measured at 100 K [6], the electronic thermal conductivities of FeSb$_2$ at 100 K along xx, yy, and zz directions are 0.168, 0.127, and 0.110
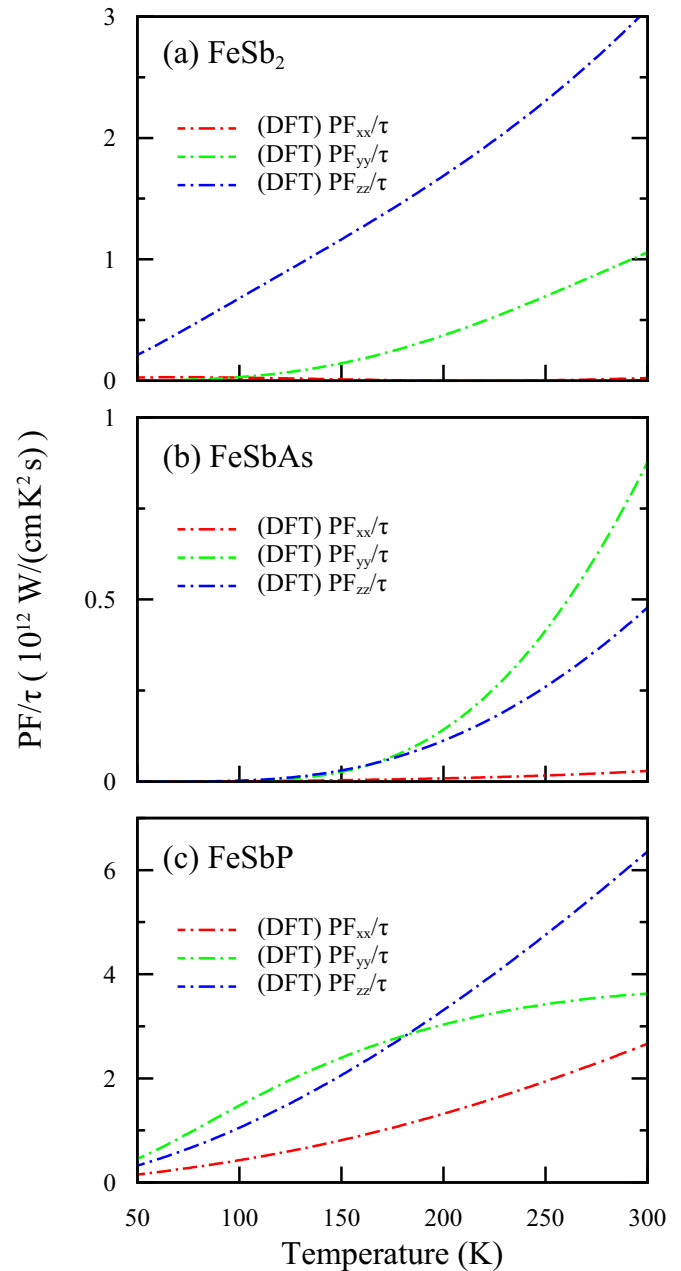

FIG. 6. Power factors divided by the relaxation time (PF/τ) (calculated by the mBJ scheme) for (a) FeSb$_2$, (b) FeSbAs, and (c) FeSbP as a function of temperature.

(0.262 for a different sample) W m^{-1} K^{-1}, respectively. Compared to the lattice thermal conductivity (κ_l) of FeSb$_2$ measured at 100 K, which is about 20–30 W m^{-1} K^{-1} [6,7], κ_e is much smaller than κ_l. Taking into account κ_l, ZT is much reduced to have the order of magnitude of $10^{-4} \sim 10^{-5}$. Therefore reducing κ_l is an ultimate goal for increasing ZT. Sun *et al.* reported that a slight substitution of As in FeSb$_2$, FeSb$_{2-x}$As$_x$ ($x = 0.03$), reduces the thermal conductivity much more up to by a factor of 5 [7]. The reduction is due to the effect of substitutional disorder.

We can estimate κ_l from the kinetic formula $\kappa_l = 1/3C(T) \cdot v_s \cdot l_p$, where $C(T)$, v_s, and l_p are the lattice specific heat,
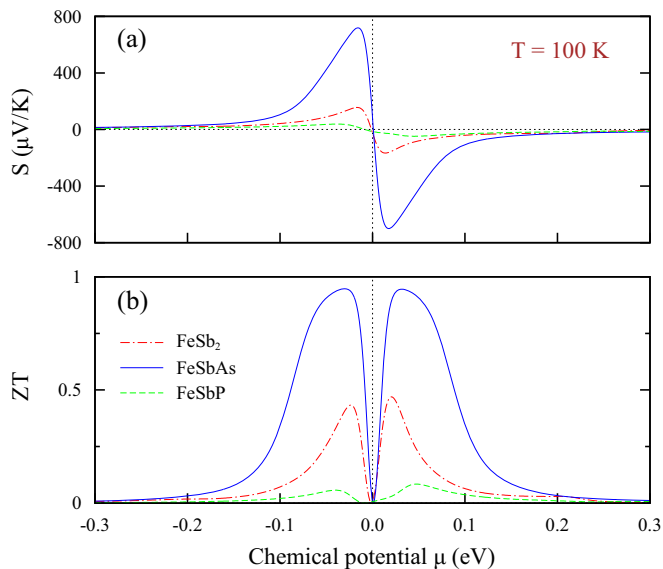
FIG. 7. Comparison in thermoelectric properties (calculated by the mBJ scheme) among FeSb$_2$, FeSbAs, and FeSbP materials at $T = 100$ K. (a) Seebeck coefficients and (b) figure of merits ZT (without considering the lattice thermal conductivities) are shown as a function of the chemical potential. These two thermoelectric properties are averaged over the three x, y, and z directions.

sound velocity, and phonon mean free path, respectively. The lattice specific heat $C(T)$ and sound velocity v_s could be calculated from a Debye model with the Debye temperature listed in Table III. With the phonon mean free path provided in Table III, the estimated lattice thermal conductivities of FeSb$_2$, FeSbAs, and FeSbP at 5 K are 257, 105, and 129 W m^{-1} K^{-1}, respectively. Scaling the measured κ_l of FeSb$_2$ at 100 K by

TABLE III. Physical parameters for FeSb$_2$, FeSbAs, and FeSbP. Effective masses of valence (m_V^*) and conduction (m_C^*) bands are calculated from the relation $(m^*)_{ij}^{-1} = \frac{1}{\hbar^2} \frac{\partial^2 E(k)}{\partial k_i k_j}$ in the unit of the rest mass of an electron. Average effective masses m_V^* and m_C^* are obtained via the harmonic mean. The Debye temperatures θ_D are obtained from the first-principle phonon calculations [50]. The sound velocities v_s are calculated from a Debye model. A phonon mean free path l_p is assumed to be proportional to an average lattice constant, that is, $l_p \propto \sqrt[3]{V}$, where V is the unit cell volume. Given $l_p = 350$ μm for FeSb$_2$ [6], l_p for FeSbAs and FeSbP could be obtained.

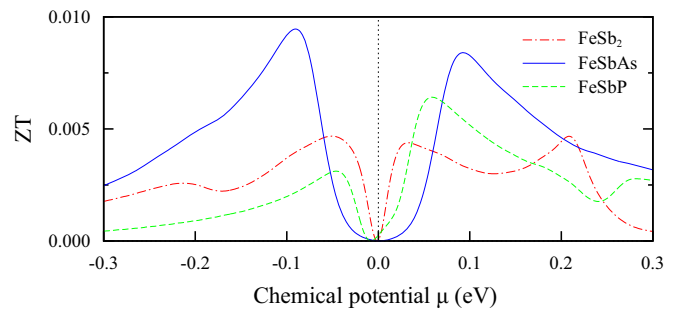|	FeSb$_2$	FeSbAs	FeSbP
$(m_V^*)_{xx}$	-0.21	-0.40	-0.79
$(m_V^*)_{yy}$	-0.34	-0.46	-0.51
$(m_V^*)_{zz}$	-0.43	-0.44	-8.97
m_V^*	-0.30	-0.43	-0.90
$(m_C^*)_{xx}$	1.43	0.82	1.19
$(m_C^*)_{yy}$	3.64	2.44	4.85
$(m_C^*)_{zz}$	1.39	0.96	1.86
m_C^*	1.77	1.12	1.90
θ_D (K)	286	476	420
v_s (m/s)	2634	3890	3581
l_p (μm)	350	311	324

FIG. 8. Figure of merits ZT at $T = 100$ K (with considering the lattice thermal conductivities) are shown as a function of the chemical potential.

the ratio of the estimated lattice thermal conductivities at 5 K, we can roughly estimate the lattice thermal conductivities of FeSbAs and FeSbP at 100 K to be $\sim$10 and $\sim$12 W m^{-1}K^{-1}, respectively. Using these values, ZT at 100 K [53] is plotted in Fig. 8. Again, the newly proposed material FeSbAs has a higher ZT than FeSb$_2$ with a chemical potential shift, which is accomplished by electron or hole doping.

We also checked the electronic structure and thermoelectric properties of FeSbAs at ambient pressure. The insulating phase cannot be obtained in the GGA(PBE) functional. The mBJ method describes the insulating phase with the band gap of 297 meV. This value is almost two times larger than that at high pressure $P = 40$ GPa. The thermoelectric power at ambient pressure is as $\sim$3.3 times large as that at high pressure (at $T \approx 80$ K), however, the electrical conductivity is reduced due to the larger band gap. It results in no substantial enhancement in PF/τ at ambient pressure.

D. Miscibility gap at ambient pressure

Since FeSb$_{1.97}$As$_{0.03}$ was experimentally synthesized and was reported to have the much more reduced thermal conductivity compared to FeSb$_2$ [7], we investigate the miscibility of FeSb$_2$ and FeAs$_2$ at ambient pressure theoretically. We take into account the miscibility of FeSb$_2$ and FeP$_2$ as well. Considering a mixture of $(1 - x)$ mole fractions of FeSb$_2$ and x mole fractions of FeAs$_2$ (FeP$_2$) producing the resultant material FeSb$_{2-2x}$As$_{2x}$ (FeSb$_{2-2x}$P$_{2x}$), the mixing energy, which is required to obtain the resultant material, is

$$\Delta E_{\text{mix}}(x) = E_f(\text{FeSb}_{2-2x}\text{X}_{2x})$$
$$- ((1-x)E_f(\text{FeSb}_2) + xE_f(\text{FeX}_2)),$$
$$(\text{where X = As or P}), \qquad (2)$$

where E_f are formation energies for the given compounds [54]. Together with the material-independent entropy of mixing $S = -\frac{R}{3}(x \ln(x) + (1-x)\ln(1-x))$, where R is the gas constant, the mixing Gibbs free energy is

$$\Delta G_{\text{mix}}(x, T) = \Delta E_{\text{mix}}(x)$$
$$+ \frac{RT}{3}(x \ln(x) + (1-x)\ln(1-x)). \quad (3)$$

The boundary of a miscibility gap [55,56], at which the entropy gain compensates the energy cost of mixing, could be obtained by minimizing Eq. (3).

Since the energy above hull for FeSbAs (32.2 meV/atom) is much smaller than that for FeSbP (204.6 meV/atom), the miscibility gap region of $FeSb_{2-2x}As_{2x}$ is quite smaller than that of $FeSb_{2-2x}P_{2x}$. We would like to note that the maximal temperature of boundary of miscibility gap for $FeSb_{2-2x}As_{2x}$ and $FeSb_{2-2x}P_{2x}$ are ~1914 and ~5980 K, respectively. It indicates that the substitution of As for Sb in $FeSb_2$ is more favorable than the substitution of P for Sb in $FeSb_2$.

IV. SUMMARY AND CONCLUSIONS

We investigated the new thermoelectric material FeSbAs, which is analogous to $FeSb_2$ in chemical and structural point of views. We checked the phase stability of FeSbAs and found that it can be made thermodynamically stable at high pressure above ~30 GPa. Another material analog FeSbP has the same crystal structure as FeSbAs, however, it is more thermodynamically unstable than FeSbAs and could not be stable even at high pressure. We also investigated electronic structures of three material analogs $FeSb_2$, FeSbAs, and FeSbP by using the mBJ method. Considering the band gap found in $FeSb_2$ experimentally, the mBJ method gives the reasonable electronic structure. Regarding $FeSb_2$ as a member of a family of compounds ($FeSb_2$, FeSbAs, and FeSbP), we identified that the octahedral rotations could control the size of the band gap in this series. We also studied the thermoelectric properties of three material analogs within our theoretical framework and found that FeSbAs has the largest Seebeck coefficient among them above 50 K. FeSbAs could also have a higher ZT than $FeSb_2$ with electron or hole doping. Hence FeSbAs should be searched experimentally. More generally, the isovalent substituting Sb with P or As should be studied. P is predicted to be much less soluble than As which indeed has been reported in the literature [7].

ACKNOWLEDGMENTS

APPENDIX: MODEL CALCULATION FOR TRANSPORT PROPERTIES

In our DFT simulations for temperature dependent transport properties, the chemical potential was fixed to the middle of the band gap. However, the chemical potential is a function of temperature. In semiconducting materials, the impurity effect also affects the temperature dependence of the chemical potential. In Appendix, we discuss the temperature behavior of the chemical potential in the presence of the impurities and the corresponding thermoelectric power [57]. We also discuss the extremum in the Seebeck coefficient versus temperature curve observed in experiments for $FeSb_2$ at low temperature.

1. Brief review: One-band model with a fixed chemical potential

First, we briefly review the one-band model with a fixed chemical potential introduced in Ref. [59]. Since the measured thermoelectric power for $FeSb_2$ has a negative sign below 50 K, the dominant charge carrier is electron-type. For simplicity, the authors of Ref. [59] considered a single conduction band model with electron-type carriers. Furthermore, they assumed a fixed (temperature independent) chemical potential $\mu = -\Delta$ (where Δ is the activation energy) and an isotropic parabolic conduction band dispersion

$$\epsilon_k = \frac{\hbar^2 k^2}{2m^*}, \tag{A1}$$

where m^* is the effective mass. Then the band velocity is obtained by the following relation

$$v_k^\alpha = \frac{1}{\hbar}\frac{\partial \epsilon_k}{\partial k_\alpha} = \frac{\hbar}{m^*}k_\alpha, \tag{A2}$$

where $\alpha = x, y, z$. Transport properties can be computed within the Boltzmann theory by the following expressions:

$$\sigma_{xx} = \frac{2e^2}{V}\sum_k\left(-\frac{\partial f}{\partial \epsilon_k}\right)v_k^x v_k^x \tau_k, \tag{A3}$$

$$\alpha_{xx} = -\frac{2e}{VT}\sum_k\left(-\frac{\partial f}{\partial \epsilon_k}\right)v_k^x v_k^x(\epsilon_k - \mu)\tau_k, \tag{A4}$$

where f and τ_k are the Fermi-Dirac distribution function and the relaxation time, respectively. The Seebeck coefficient can then easily be calculated:

$$S = \frac{\alpha_{xx}}{\sigma_{xx}}. \tag{A5}$$

Using the fact that the summation of k could be changed into the integral of energy ϵ with the density of states $D(\epsilon)$, that is, $\sum_k \to \int_{-\infty}^{\infty} d\epsilon\, D(\epsilon)$, Eqs. (A3) and (A4) could be rewritten as

$$\sigma_{xx} = \frac{4e^2}{3V}\frac{\tau_0}{m^*}\int_{-\infty}^{\infty} d\epsilon\, D(\epsilon)\left(-\frac{\partial f}{\partial \epsilon}\right)\epsilon, \tag{A6}$$

$$\alpha_{xx} = -\frac{4e}{3VT}\frac{\tau_0}{m^*}\int_{-\infty}^{\infty} d\epsilon\, D(\epsilon)\left(-\frac{\partial f}{\partial \epsilon}\right)\epsilon(\epsilon + \Delta), \tag{A7}$$

where the (direction independent) constant relaxation time approximation $\tau_k \approx \tau_0$ is used. The density of states for the parabolic energy dispersion of Eq. (A1) is

$$D(\epsilon) = V\frac{(2m^*)^{3/2}}{2\pi^2\hbar^3}\epsilon^{1/2} \quad (\epsilon > 0), \tag{A8}$$

hence we can estimate Eqs. (A6) and (A7) for two different limiting cases: $\Delta \gg k_B T$ and $\Delta \ll k_B T$.

(i) When $\Delta \gg k_B T$,

$$\sigma_{xx} \simeq \left(\frac{k_B T}{\pi}\right)^{3/2}\frac{e^2(2m^*)^{1/2}\tau_0}{\hbar^3}\exp\left(\frac{-\Delta}{k_B T}\right),$$

$$\alpha_{xx} \simeq -\frac{e(2m^*)^{1/2}\tau_0}{\pi^{3/2}\hbar^3 T}(k_B T)^{5/2}\exp\left(\frac{-\Delta}{k_B T}\right)\left(\frac{\Delta}{k_B T} + \frac{5}{2}\right),$$

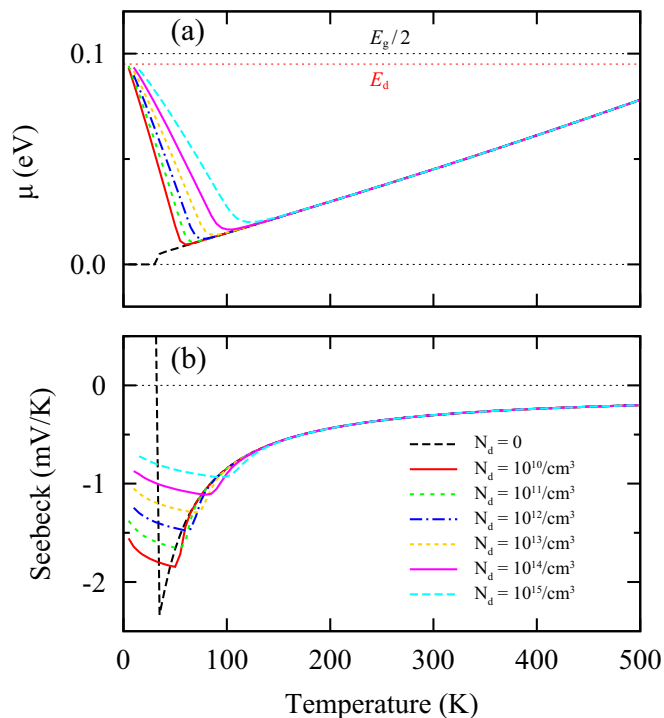$$S \simeq -\frac{k_B}{e}\left(\frac{\Delta}{k_B T} + \frac{5}{2}\right). \tag{A9}$$

FIG. 9. Two-band model for thermoelectric properties with ionized donor impurities. We set a band gap $E_g = 0.2$ eV, donor impurity level $E_d = 95$ meV, valence and conduction band effective masses $m_{\mathrm{VB}}^* = 10\,m_0$, $m_{\mathrm{CB}}^* = m_0$ (where m_0 is the electron rest mass), and cell volume $V = 123.673$ Å^3. (a) Chemical potential μ and (b) Seebeck coefficient as a function of temperature for different donor impurity concentrations.

(ii) When $\Delta \ll k_B T$,

$$\sigma_{xx} \simeq \left(\frac{k_B T}{\pi}\right)^{3/2} \frac{e^2 (m^*)^{1/2} \tau_0}{\hbar^3} (\sqrt{2} - 1)\zeta\left(\frac{3}{2}\right),$$

$$\alpha_{xx} \simeq -\left(\frac{k_B T}{\pi}\right)^{3/2} \frac{e (m^*)^{1/2} \tau_0}{\hbar^3 T}\left[(\sqrt{2} - 1)\zeta\left(\frac{3}{2}\right)\Delta \right.$$
$$\left. + \frac{5}{4}(2\sqrt{2} - 1)\zeta\left(\frac{5}{2}\right)k_B T\right],$$

$$S \simeq -\frac{k_B}{e}\left(\frac{\Delta}{k_B T} + \frac{5(2\sqrt{2} - 1)\zeta(5/2)}{4(\sqrt{2} - 1)\zeta(3/2)}\right)$$
$$\simeq -\frac{k_B}{e}\left(\frac{\Delta}{k_B T} + 2.833442009\ldots\right), \qquad (A10)$$

where $\zeta(x)$ is the Riemann zeta function. Note that the Seebeck coefficient S is independent of the relaxation time τ_0 in this approximation. For both limiting cases, the Seebeck coefficient is proportional to the inverse of temperature and does not show the extremum, whereas it does in experiments.

2. Two-band model

In this section, we discuss the two-band model consisting of one valence and one conduction band with a band gap of E_g. For convenience, we assume simple parabolic band dispersions for both valence and conduction bands and positions of the
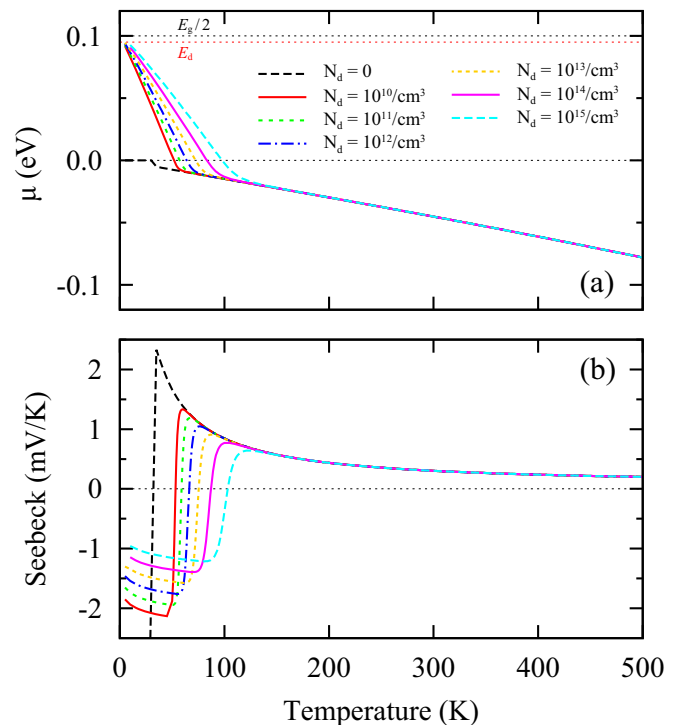
FIG. 10. Same as Fig. 9 except for different valence and conduction band effective masses in the two-band model. We set $m_{\mathrm{VB}}^* = m_0$ and $m_{\mathrm{CB}}^* = 10\,m_0$.

valence band maximum and the conduction band minimum are $-E_g/2$ and $E_g/2$, respectively, in order for the middle point of the band gap to be zero. Then, the valence- and conduction-band dispersions are

$$\epsilon_k^{\mathrm{VB}} = -E_g/2 - \frac{\hbar^2 k^2}{2m_{\mathrm{VB}}^*},$$

$$\epsilon_k^{\mathrm{CB}} = E_g/2 + \frac{\hbar^2 k^2}{2m_{\mathrm{CB}}^*}, \qquad (A11)$$

where m_{VB}^* and m_{CB}^* are the valence and conduction band effective mass, respectively, and density of states for the valence and conduction bands are

$$D^{\mathrm{VB}}(\epsilon) = V\frac{(2m_{\mathrm{VB}}^*)^{3/2}}{2\pi^2\hbar^3}(-\epsilon - E_g/2)^{1/2},$$

$$D^{\mathrm{CB}}(\epsilon) = V\frac{(2m_{\mathrm{CB}}^*)^{3/2}}{2\pi^2\hbar^3}(\epsilon - E_g/2)^{1/2}. \qquad (A12)$$

To demonstrate that the Seebeck coefficient of FeSb$_2$ has a negative sign and the extremum at low temperature in experiments, we allow the temperature dependent chemical potential and the presence of ionized donor impurities. (The ionized acceptor impurities make the Seebeck coefficient positive at low temperature, which is not the case for FeSb$_2$.) The occupation of ionized donor impurities is

$$N_{d^+} = \frac{N_d}{1 + 2\exp(-(E_d - \mu)/k_B T)} \qquad (A13)$$

with donor concentration N_d and donor impurity level E_d.

Occupations of electron (n) and hole (p) are

$$n = \int_{E_g/2}^{\infty} d\epsilon\, D^{CB}(\epsilon) f(\epsilon),$$

$$p = \int_{-\infty}^{-E_g/2} d\epsilon\, D^{VB}(\epsilon)(1 - f(\epsilon)). \tag{A14}$$

Then the condition of the charge neutrality $n = p + N_{d^+}$ determines the position of the chemical potential μ, which is usually as a function of temperature as shown in Figs. 9(a) and 10(a). In the intrinsic case, $N_d = 0$, the chemical potential is almost temperature independent and very close to the middle of the band gap at low temperature. Above a certain temperature, the chemical potential shows the linear dependence of temperature and its slope is determined by the valence and conduction band effective masses m_{VB}^* and m_{CB}^*. When $m_{VB}^* > m_{CB}^*$ [see Fig. 9(a)], the linear slope is positive, hence the chemical potential is close to the conduction band upon heating. On the other hand, when $m_{VB}^* < m_{CB}^*$

[see Fig. 10(a)], the linear slope is negative, that is, the chemical potential is far away from the conduction band upon heating.

The presence of the ionized donor impurity makes the chemical potential close to the conduction band at low temperature. Up to a certain temperature the chemical potential goes down to the middle of the band gap upon heating, and then follows the intrinsic high-temperature slope regardless of the donor impurity concentrations.

Using the obtained temperature dependent chemical potential and Eqs. (A3)–(A5), we can obtain the Seebeck coefficient as a function of temperature and the result is shown in Figs. 9(b) and 10(b). At finite donor impurity concentrations, the Seebeck coefficients show an extremum and the position of the extremum is changed depending on the impurity concentration. The remarkable difference between Figs. 9(b) and 10(b) is that at finite impurity concentrations the Seebeck coefficient changes the sign only for $m_{VB}^* < m_{CB}^*$ and shows another extremum upon heating [60].

---

[1] D. M. Rowe and C. M. Bhandari, *Modern Thermoelectrics* (Reston Publishing, Reston, Virginia, 1983).

[2] G. D. Mahan and J. O. Sofo, Proc. Natl. Acad. Sci. U.S.A. **93**, 7436 (1996).

[3] G. D. Mahan, Solid State Phys. **51**, 81 (1998).

[4] T. Saso and K. Urasaki, J. Phys. Chem. Solids **63**, 1475 (2002).

[5] C. Grenzebach and G. Czycholl, Physica B (Amsterdam) **359–361**, 732 (2005).

[6] A. Bentien, S. Johnsen, G. K. M. Madsen, B. B. Iversen, and F. Steglich, Europhys. Lett. **80**, 17008 (2007).

[7] P. Sun, N. Oeschler, S. Johnsen, B. B. Iversen, and F. Steglich, Dalton Trans. **39**, 1012 (2010).

[8] J. M. Tomczak, K. Haule, T. Miyake, A. Georges, and G. Kotliar, Phys. Rev. B **82**, 085104 (2010).

[9] M. S. Diakhate, R. P. Hermann, A. Möchel, I. Sergueev, M. Søndergaard, M. Christensen, and M. J. Verstraete, Phys. Rev. B **84**, 125210 (2011).

[10] C. Herring, Phys. Rev. **96**, 1163 (1954).

[11] H. Takahashi, R. Okazaki, S. Ishiwata, H. Taniguchi, A. Okutani, M. Hagiwara, and I. Terasaki, Nat. Commun. **7**, 12732 (2016).

[12] M. Battiato, J. M. Tomczak, Z. Zhong, and K. Held, Phys. Rev. Lett. **114**, 236603 (2015).

[13] G. Hautier, S. P. Ong, A. Jain, C. J. Moore, and G. Ceder, Phys. Rev. B **85**, 155208 (2012).

[14] S. Kirklin, J. E. Saal, B. Meredig, A. Thompson, J. W. Doak, M. Aykol, S. Rühl, and C. Wolverton, Comp. Mater. **1**, 15010 (2015).

[15] A. Jain, S. P. Ong, G. Hautier, W. Chen, W. D. Richards, S. Dacek, S. Cholia, D. Gunter, D. Skinner, G. Ceder, and K. A. Persson, APL Mater. **1**, 011002 (2013).

[16] W. Setyawan, R. M. Gaume, S. Lam, R. S. Feigelson, and S. Curtarolo, ACS Comb. Sci. **13**, 382 (2011).

[17] J. H. Shim, K. Haule, and G. Kotliar, Phys. Rev. B **79**, 060501(R) (2009).

[18] N. Katayama, K. Kudo, S. Onari, T. Mizukami, K. Sugawara, Y. Sugiyama, Y. Kitahama, K. Iba, K. Fujimura, N. Nishimoto, M. Nohara, and H. Sawa, J. Phys. Soc. Jpn. **82**, 123702 (2013).

[19] C.-J. Kang, T. Birol, and G. Kotliar, Phys. Rev. B **95**, 014511 (2017).

[20] D. Duan, Y. Liu, F. Tian, D. Li, X. Huang, Z. Zhao, H. Yu, B. Liu, W. Tian, and T. Cui, Sci. Rep. **4**, 6968 (2014).

[21] A. P. Drozdov, M. I. Eremets, I. A. Troyan, A. Ksenofontov, and S. I. Shylin, Nature (London) **525**, 73 (2015).

[22] X. Zhang, L. Yu, A. Zakutayev, and A. Zunger, Adv. Funct. Mater. **22**, 1425 (2012).

[23] F. Yan, X. Zhang, Y. G. Yu, L. Yu, A. Nagaraja, T. O. Mason, and A. Zunger, Nat. Commun. **6**, 7308 (2015).

[24] R. Gautier, X. Zhang, L. Hu, L. Yu, Y. Lin, T. O. L. Sunde, D. Chon, K. R. Poeppelmeier, and A. Zunger, Nat. Chem. **7**, 308 (2015).

[25] Q. Hu, D. Y. Kim, W. Yang, L. Yang, Y. Meng, L. Zhang, and H.-K. Mao, Nature (London) **534**, 241 (2016).

[26] Y.-L. Li, S.-N. Wang, A. R. Oganov, H. Gou, J. S. Smith, and T. A. Strobel, Nat. Commun. **6**, 6974 (2015).

[27] X. Dong, A. R. Oganov, A. F. Goncharov, E. Stavrou, S. Lobanov, G. Saleh, G.-R. Qian, Q. Zhu, C. Gatti, V. L. Deringer, R. Dronskowski, X.-F. Zhou, V. B. Prakapenka, Z. Konôpková, I. A. Popov, A. I. Boldyrev, and H.-T. Wang, Nat. Chem. **9**, 440 (2017).

[28] A. Jain, Y. Shin, and K. A. Persson, Nat. Rev. Mater. **1**, 15004 (2016).

[29] A. R. Oganov and C. W. Glass, J. Chem. Phys. **124**, 244704 (2006).

[30] C. W. Glass, A. R. Oganov, and N. Hansen, Comput. Phys. Commun. **175**, 713 (2006).

[31] G. Kresse and J. Furthmüller, Comput. Mater. Sci. **6**, 15 (1996).

[32] G. Kresse and J. Furthmüller, Phys. Rev. B **54**, 11169 (1996).

[33] J. P. Perdew, K. Burke, and M. Ernzerhof, Phys. Rev. Lett. **77**, 3865 (1996).

[34] P. E. Blöchl, Phys. Rev. B **50**, 17953 (1994).

[35] G. Kresse and D. Joubert, Phys. Rev. B **59**, 1758 (1999).

[36] N. Lanatà, Y. Yao, C.-Z. Wang, K.-M. Ho, and G. Kotliar, Phys. Rev. X **5**, 011008 (2015).

[37] http://ykent.public.iastate.edu/cygutz/

[38] P. Blaha, K. Schwarz, G. K. H. Madsen, D. Kavasnicka, and J. Luitz, WIEN2K (Karlheinz Schwarz, Technische Universitat Wien, Austria, 2001).

[39] J. M. Tomczak, K. Haule, and G. Kotliar, Proc. Natl. Acad. Sci. U.S.A. **109**, 3243 (2012).

[40] Z. P. Yin, K. Haule, and G. Kotliar, Nat. Phys. **7**, 294 (2011).

[41] F. Tran and P. Blaha, Phys. Rev. Lett. **102**, 226401 (2009).

[42] G. K. H. Madsen and D. J. Singh, Comput. Phys. Commun. **175**, 67 (2006).

[43] T. Rosenqvist, Acta Metall. **1**, 761 (1953).

[44] S. P. Ong, L. Wang, B. Kang, and G. Ceder, Chem. Mater. **20**, 1798 (2010).

[45] S. P. Ong, A. Jain, G. Hautier, B. Kang, and G. Ceder, Electrochem. Commun. **12**, 427 (2010).

[46] http://pymatgen.org/

[47] C. Petrovic, J. W. Kim, S. L. Bud'ko, A. I. Goldman, P. C. Canfield, W. Choe, and G. J. Miller, Phys. Rev. B **67**, 155205 (2003).

[48] A. Perucchi, L. Degiorgi, R. Hu, C. Petrovic, and V. F. Mitrović, Eur. Phys. J. B **54**, 175 (2006).

[49] A. V. Lukoyanov, V. V. Mazurenko, V. I. Anisimov, M. Sigrist, and T. M. Rice, Eur. Phys. J. B **53**, 205 (2006).

[50] For phonon calculations, we have used the linear response method [51] implemented in the QUANTUM ESPRESSO code [52]. PW91 ultrasoft pseudopotentials were used for all atoms. We used a $15 \times 15 \times 15\,k$ grid and a Hermite-Gaussian smearing of 0.03 Ry for the electronic integration. The dynamical matrices were calculated on a $2 \times 2 \times 2$ phonon-momentum grid.

[51] S. Baroni, S. de Gironcoli, A. D. Corso, and P. Giannozzi, Rev. Mod. Phys. **73**, 515 (2001).

[52] P. Giannozzi *et al.*, J. Phys.: Condens. Matter **21**, 395502 (2009).

[53] The relaxation time (τ) for FeSb$_2$ is obtained from the measured κ_e and calculated κ_e/τ. We assume that relaxation times for FeSb$_2$, FeSbAs, and FeSbP are almost identical.

[54] The formation energies for FeSb$_2$, FeSbAs (FeSbP), and FeAs$_2$ (FeP$_2$) are calculated by the VASP GGA(PBE) functional and then those for intermediate concentrations of FeSb$_{2-2x}$As$_{2x}$ (FeSb$_{2-2x}$P$_{2x}$) are obtained by interpolation.

[55] S. Bhattacharya and G. K. H. Madsen, Phys. Rev. B **92**, 085205 (2015).

[56] R. Chmielowski, S. Bhattacharya, S. Jacob, D. Péré, A. Jacob, K. Moriya, B. Delatouche, P. Roussel, G. Madsen, and G. Dennler, Sci. Rep. **7**, 46630 (2017).

[57] We do not consider the electron-phonon coupling that could affect the transport properties. Note that the sizable electron-phonon coupling is measured from polarized Raman scattering spectra of the Fe$_{1-x}$Co$_x$Sb$_2$ and Fe$_{1-x}$Cr$_x$Sb$_2$ single crystals [58].

[58] N. Lazarević, Z. V. Popović, R. Hu, and C. Petrovic, Phys. Rev. B **81**, 144302 (2010).

[59] P. Sun, W. Xu, J. M. Tomczak, G. Kotliar, M. Søndergaard, B. B. Iversen, and F. Steglich, Phys. Rev. B **88**, 245203 (2013).

[60] In case of the presence of the ionized acceptor impurity (p-type doping), the opposite behavior is expected. When $m^*_{VB} > m^*_{CB}$, the Seebeck coefficient changes the sign from a positive to a negative value upon heating. When $m^*_{VB} < m^*_{CB}$, the Seebeck coefficient always has a positive value for a finite impurity concentration.